

RELATION BETWEEN BLACK HOLE MASS AND BULGE LUMINOSITY IN HARD X-RAY SELECTED TYPE 1 AGNS

SUYEON SON¹, MINJIN KIM¹, AARON J. BARTH², AND LUIS C. HO^{3,4}

¹Department of Astronomy and Atmospheric Sciences, College of Natural Sciences, Kyungpook National University, Daegu 41566, Korea; mkim.astro@gmail.com

²Department of Physics and Astronomy, University of California, Irvine, CA 92697-4575, USA

³Kavli Institute for Astronomy and Astrophysics, Peking University, Beijing 100871, China

⁴Department of Astronomy, School of Physics, Peking University, Beijing 100871, China

Received —; accepted —

Abstract: Using I -band images of 35 nearby ($z < 0.1$) type 1 active galactic nuclei (AGNs) obtained with *Hubble Space Telescope*, selected from the 70-month Swift-BAT X-ray source catalog, we investigate the photometric properties of the host galaxies. With a careful treatment of the point-spread function (PSF) model and imaging decomposition, we robustly measure the I -band brightness and the effective radius of bulges in our sample. Along with black hole (BH) mass estimates from single-epoch spectroscopic data, we present the relation between BH mass and I -band bulge luminosity ($M_{\text{BH}}-M_{I,\text{bul}}$ relation) of our sample AGNs. We find that our sample lies offset from the $M_{\text{BH}}-M_{I,\text{bul}}$ relation of inactive galaxies by 0.4 dex, i.e., at a given bulge luminosity, the BH mass of our sample is systematically smaller than that of inactive galaxies. We also demonstrate that the zero point offset in the $M_{\text{BH}}-M_{I,\text{bul}}$ relation with respect to inactive galaxies is correlated with the Eddington ratio. Based on the Kormendy relation, we find that the mean surface brightness of ellipticals and classical bulges in our sample is comparable to that of normal galaxies, revealing that bulge brightness is not enhanced in our sample. As a result, we conclude that the deviation in the $M_{\text{BH}}-M_{I,\text{bul}}$ relation from inactive galaxies is possibly because the scaling factor in the virial BH mass estimator depends on the Eddington ratio.

Key words: black hole physics — galaxies: active — galaxies: Seyfert — quasars

1. INTRODUCTION

Supermassive black holes (SMBHs) are ubiquitous at the centers of massive galaxies, and their mass is tightly correlated with various physical properties of bulges, such as luminosity, stellar mass, and velocity dispersion (Kormendy & Ho 2013). While these scaling relations imply a physical connection between SMBH and the host galaxy in terms of their formation and evolution, the physical origin of the scaling relations is still under debate. Energetic feedback from an active galactic nucleus (AGN) is one of the favored mechanisms to drive the co-evolution of SMBH and the host galaxy (e.g., Di Matteo et al. 2005). In this light, exploring the scaling relations in AGN is of great importance to unveil the origin of the BH-host relations.

Several scaling relations have been widely used to understand the causal connection between SMBHs and their host galaxies in active galaxies, thanks to the relative ease of estimating the BH mass of type 1 AGN, which exhibit blue continuum from the accretion disk and broad emission lines in the spectrum. For example, using the relation between BH mass and physical properties of the bulge (e.g., stellar velocity dispersion and bulge luminosity) from distant AGNs, previous studies argued that BH growth precedes galaxy growth (e.g., Peng et al. 2006; Woo et al. 2008; Park et al. 2014). Us-

ing AGN in the local universe, several studies reported that active galaxies deviate from inactive galaxies in the $M_{\text{BH}}-M_{\text{bul}}$ relation, revealing that either BH mass is systematically undermassive or bulge luminosity is overluminous compared to normal galaxies (e.g., Kim et al. 2008b; Kim & Ho 2019).

On the other hand, a relation between the effective radius and the mean surface brightness within the effective radius (Kormendy relation; Kormendy 1977) has been extensively used to probe young stellar populations in host galaxies of nearby AGNs (e.g., Kim & Ho 2019; Zhao et al. 2019, 2021). For example, Kim & Ho (2019) argued that bulges regardless of the bulge types in galaxies hosting type 1 AGNs tend to be brighter than normal galaxies inferred from the Kormendy relation, possibly due to recent star formation. However, using the same relation, Zhao et al. (2021) demonstrated that only pseudo-bulges in active galaxies are overluminous. Interestingly, this trend is consistent with the result for type 2 AGNs in Zhao et al. (2019). Overall, different studies reached somewhat different conclusions regarding the stellar population in galaxies hosting AGNs, possibly due to the diverse sample properties and filters (R and I) used in the previous studies (e.g., Zhao et al. 2019).

Nevertheless, previous studies for nearby AGNs included some distant AGNs ($z \leq 0.35 - 0.5$), which can still be affected by cosmic evolution (e.g., Bennert et

CORRESPONDING AUTHOR: M. Kim

al. 2010; Park et al. 2014). Additionally, the sample was dominated by AGNs selected from the UV/optical survey (e.g., Schmidt & Green 1983; Lyke et al. 2020), possibly biased toward bright and less obscured AGNs. These factors can introduce some unknown biases in establishing the BH–host relation. In this study, we make use of relatively unbiased and nearby AGNs ($z < 0.1$) drawn from a hard X-ray survey (Koss et al. 2017). Moreover, the imaging data used in this study is obtained with uniform and consistent observations, which can allow us to explore the BH–host relation with a minimum bias due to the sample selection, cosmic evolution, and diverse imaging quality.

In this study, we revisit two scaling relations (BH mass–bulge luminosity and Kormendy relations) of nearby type 1 AGNs using I -band images obtained with *Hubble Space Telescope* (*HST*). In §2, we present the physical properties of the sample, and description of the observation and data reduction. In §3, we present the methods for the imaging decomposition. We present $M_{\text{BH}}-M_{I,\text{bul}}$ and Kormendy relations of our sample by comparing them with inactive galaxies in §4. In §5, we discuss the physical origins of systematic offsets in the scaling relations. A summary and conclusions are given in §6. We adopt the following cosmological parameters: $H_0 = 100h = 67.8 \text{ km s}^{-1} \text{ Mpc}^{-1}$, $\Omega_m = 0.308$, and $\Omega_\Lambda = 0.692$ (Planck Collaboration et al. 2016).

2. SAMPLE AND DATA

2.1. Sample

Our sample contains nearby AGNs ($z < 0.1$) drawn from the 70-month Swift-BAT X-ray source catalog (Koss et al. 2017). We utilized images obtained with *HST* as a part of the gap-filler snapshot program (HST program 15444), in which the imaging survey of nearby hard X-ray selected AGNs was conducted (Kim et al. 2021). Due to less severe attenuation in the hard X-ray band, the parent sample is thought to be relatively unbiased in terms of obscuration, making the Swift-BAT sample ideal to study the physical connection between unobscured (type 1) and obscured (type 2) AGNs. The main purpose of the *HST* survey is to study the photometric properties of the host and their connection with the properties of AGNs. Thus, the sample for the survey was selected to contain nearby AGNs ($z < 0.1$). Owing to its uniform selection and proximity, the *HST* images of the sample are suitable to achieve the goal in this study, investigating the relation between the BH mass and bulge luminosity.

In this light, we only included objects with spectroscopic measurements of broad emission lines (type 1 AGNs). Type 1.8/1.9 AGNs are excluded because the physical properties of their broad line regions are distinct from those in canonical type 1 AGNs, which can introduce systematic uncertainty in the BH mass measurement (e.g., Ho 2008). Imaging data from program 15444 obtained before May 2020 are utilized in this study. Our final sample, originally drawn from Koss et al. (2017), consists of 35 objects with a median

redshift of ~ 0.046 and median bolometric luminosity of $\sim 10^{44.9} \text{ erg s}^{-1}$ (see Tables 1 and 2). The bolometric luminosity is inferred from the intrinsic hard X-ray luminosity (see §2.3).

2.2. Observations and Data Reduction

The *HST* images were taken with the Wide Field Channel (WFC) of the Advanced Camera for Surveys (ACS). Its field of view ($202'' \times 202''$) is large enough to cover the target galaxies. To avoid contamination from the extended emission and maximize the light ratio of the host to the nucleus, we adopted the F814W filter, corresponding to I -band. We obtained two dithered images with an exposure time of 337 s for efficient removal of cosmic rays and correction for hot pixels. An additional image with an exposure of 5 s was acquired for each target to avoid the saturation of the bright nucleus.

The basic data reduction, which includes bias subtraction, flat-fielding, and correction for the charge-transfer efficiency, was performed using the Pyraf-based STSDAS package. Cosmic rays were removed from each exposure by adopting the l.a.cosmic algorithm developed by van Dokkum (2001). The spatial offset between the two long exposures was computed using the `TweakReg` task, and the two exposures were combined after the distortion correction using `AstroDrizzle`. The pixel size in the combined image is $0.''05$. The sub-array images with short exposure time suffer heavily from a strong pattern noise in the bias, leaving a series of stripes in the raw images. To solve this problem, we removed this noise using `ACS_DESTRIPE_PLUS` (Grogan 2010). The saturated pixels at the AGN core in the long-exposure images were replaced by the corresponding pixels in the short-exposure images. Details of the observations and data reduction are described in Kim et al. (2021).

2.3. BH mass and Eddington Ratio

If the gas in the broad line region (BLR) is virialized, BH mass can be estimated from the combination of the velocity dispersion (σ) and the radius of the BLR (R_{BLR}) as $M_{\text{BH}} = f\sigma^2 R_{\text{BLR}}/G$, where f is a scaling factor determined by the kinematics and structure of the BLR. Due to the tight correlation between R_{BLR} and AGN luminosity, AGN luminosity can be a surrogate for R_{BLR} (Kaspi et al. 2000; Bentz et al. 2013; but see Du et al. 2016; Fonseca Alvarez et al. 2020). Therefore, BH mass can be computed with the width and luminosity of the broad emission lines ($\text{H}\beta$ and $\text{H}\alpha$ in this study) derived from single-epoch spectra. However, the scaling factor (f) is somewhat uncertain and has been empirically determined by assuming that, for example, active galaxies follow the same BH mass–stellar velocity dispersion relation of inactive galaxies. Ho & Kim (2015) argued that the scaling factor (f) depends on the bulge types (i.e., classical bulge vs. pseudo-bulge). Therefore, in this study, we adopted two different scaling factors for the BH mass estimation according to their bulge types. We utilize the fluxes and widths of the broad $\text{H}\alpha$ emission, estimated from the decomposition of the optical

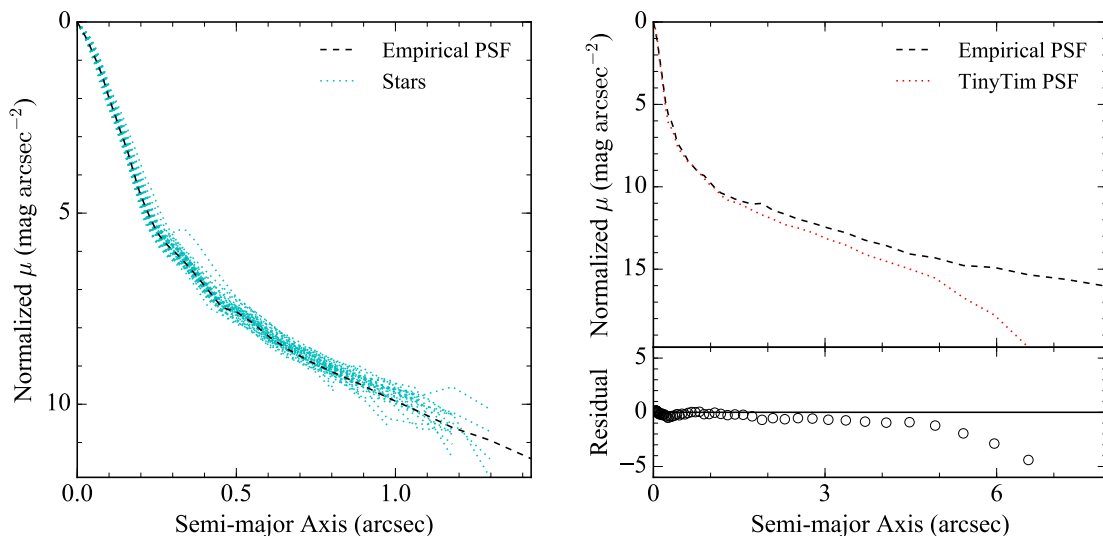


Figure 1. Surface brightness profiles of various PSFs. In the left panel, the central part of the empirical PSF and those of individual stars are represented by a black dashed line and cyan dotted lines, respectively. In the top-right panel, the profiles of the empirical PSF and TinyTim PSF are shown in black dashed line and red dotted line, respectively. The residuals are shown in the bottom-right panel.

spectra (Koss et al. 2017). If the broad $H\alpha$ emission is unavailable, we instead used the spectral measurements of broad $H\beta$ emission. The conversion from the fluxes of broad emission lines to the luminosity at 5100 \AA was performed using the conversion factors from Greene & Ho (2005). The typical uncertainty on virial mass estimates is of ~ 0.4 dex (e.g., Vestergaard & Peterson 2006).

Bolometric luminosities of AGNs are inferred from the hard X-ray luminosity estimated in the 14–195 keV band, corrected for absorption (Ricci et al. 2017). For the bolometric correction, we adopted a single conversion factor of 8 (i.e., $L_{\text{bol}} = 8 \times L_{14-195\text{keV}}$; Ricci et al. 2017). The median Eddington ratio of the entire sample is 0.06.

3. ANALYSIS

3.1. PSF Generation

To robustly estimate the bulge brightness in the images of type 1 AGNs, a careful decomposition of the bright nuclear component, modeled by a PSF, is essential. The PSF can be constructed in two different ways: (1) an empirical PSF derived from stars obtained in the same observing condition (e.g., filters and detectors); (2) a synthetic PSF modeled by TinyTim software (TinyTim PSF; Krist et al. 2011). The TinyTim PSF has been widely used as it represents the central part of the PSF relatively well. However, it often underestimates the surface brightness in the halo of the PSF, which can naturally lead to the miscalculation of underlying host brightness (e.g., Kim et al. 2008a; Zhao et al. 2021). Therefore, in this study, we employed an empirical PSF to model the nucleus.

To generate the empirical PSF, we initially selected numerous sufficiently bright but unsaturated stars from

the science images. Then, through visual inspection, extended sources and stars with close neighbors are manually excluded, finally with 44 stars remaining. We use IRAF to eliminate faint nearby sources around the target stars, adjust the scale among them, and combine the images for generating the PSF. By comparing the surface brightness profile of the generated PSF and those of individual stars obtained with *ELLIPSE* within IRAF, we confirmed that the profile in the central part of the PSF is well represented by the empirical PSF (Fig. 1). However, the wing of the PSF is rather dominated by noise, which can easily mimic the signal from the host galaxy. Therefore, to characterize the outer part of the PSF, we additionally utilized a moderately saturated star. To determine the relative scaling between the initial PSF and the saturated star, we modeled the 2D surface brightness profiles of both objects with the profile of the initial PSF using *GALFIT* (Peng et al. 2002, 2010). During the fit, the saturated pixels and charge-bleeding regions near the PSF core were properly masked out. Finally, we constructed the full PSF by replacing the masked region in the image of the saturated star with the scaled initial PSF.

To validate the empirical PSF, we compared its surface brightness profile with that of the TinyTim PSF (Fig. 1). Although two PSFs are in good agreement with each other in the central region, we found that there are substantial differences between the two PSFs in the extended wings at $r > 1''$, as expected. This comparison demonstrates that the empirical PSF is more suitable for our study.

3.2. Image Decomposition

To investigate the photometric properties of bulges in our sample, we performed a 2D imaging decomposi-

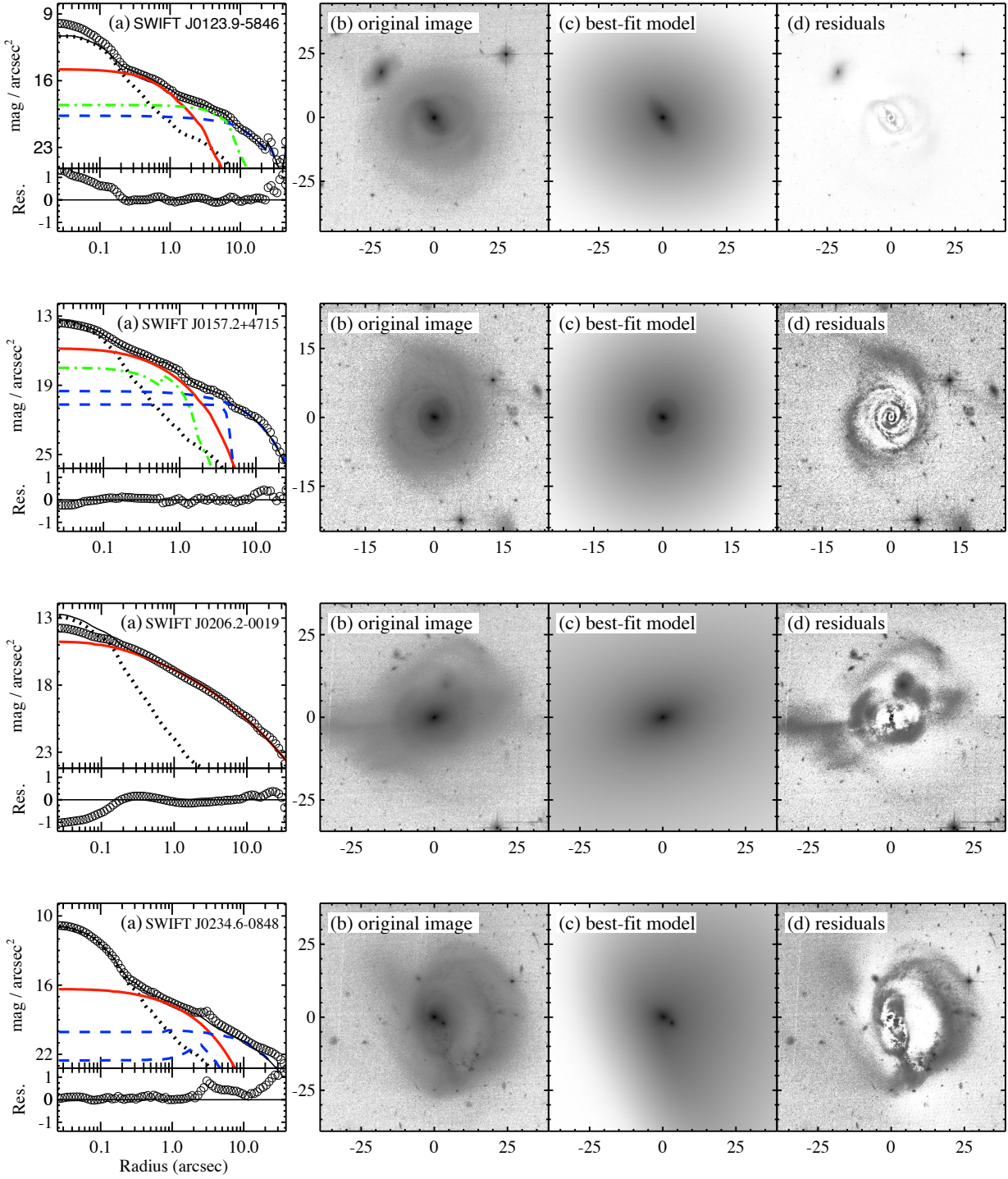


Figure 2. Results of imaging decomposition with GALFIT. (a) In the top panel, surface brightness profiles of the original image (open circles), nucleus (dotted line), and bulge (red line) are displayed. If present, bar and disk are denoted by green dashed-dotted line and blue dashed line, respectively. Black solid line represents the surface brightness profile of the best-fit model. The bottom panel shows the residual. (b) Original image. (c) Best-fit model for the host galaxy without the nuclear component. (d) Residual image. All the images are shown with an asinh stretch.

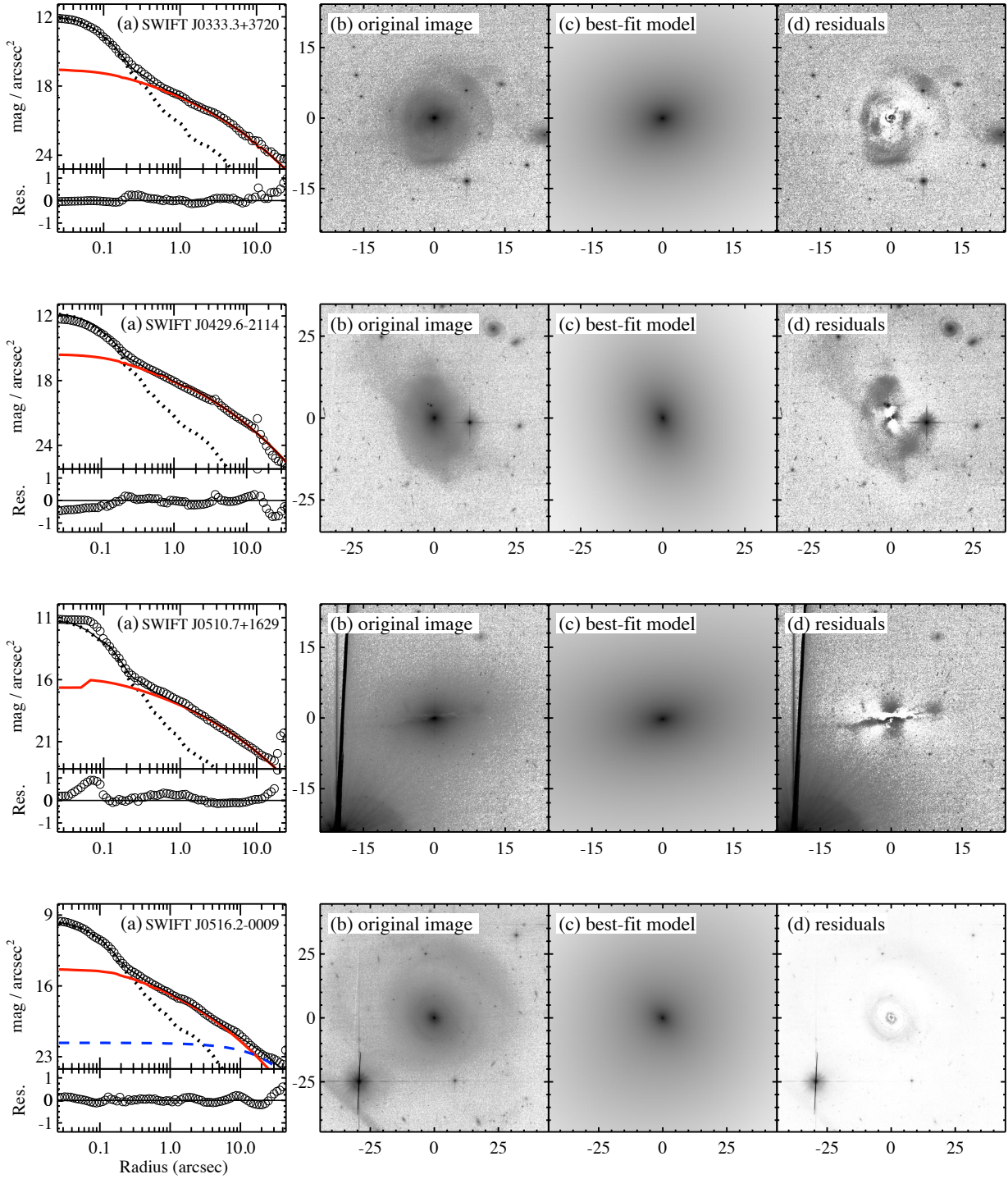


Figure 2. Continued

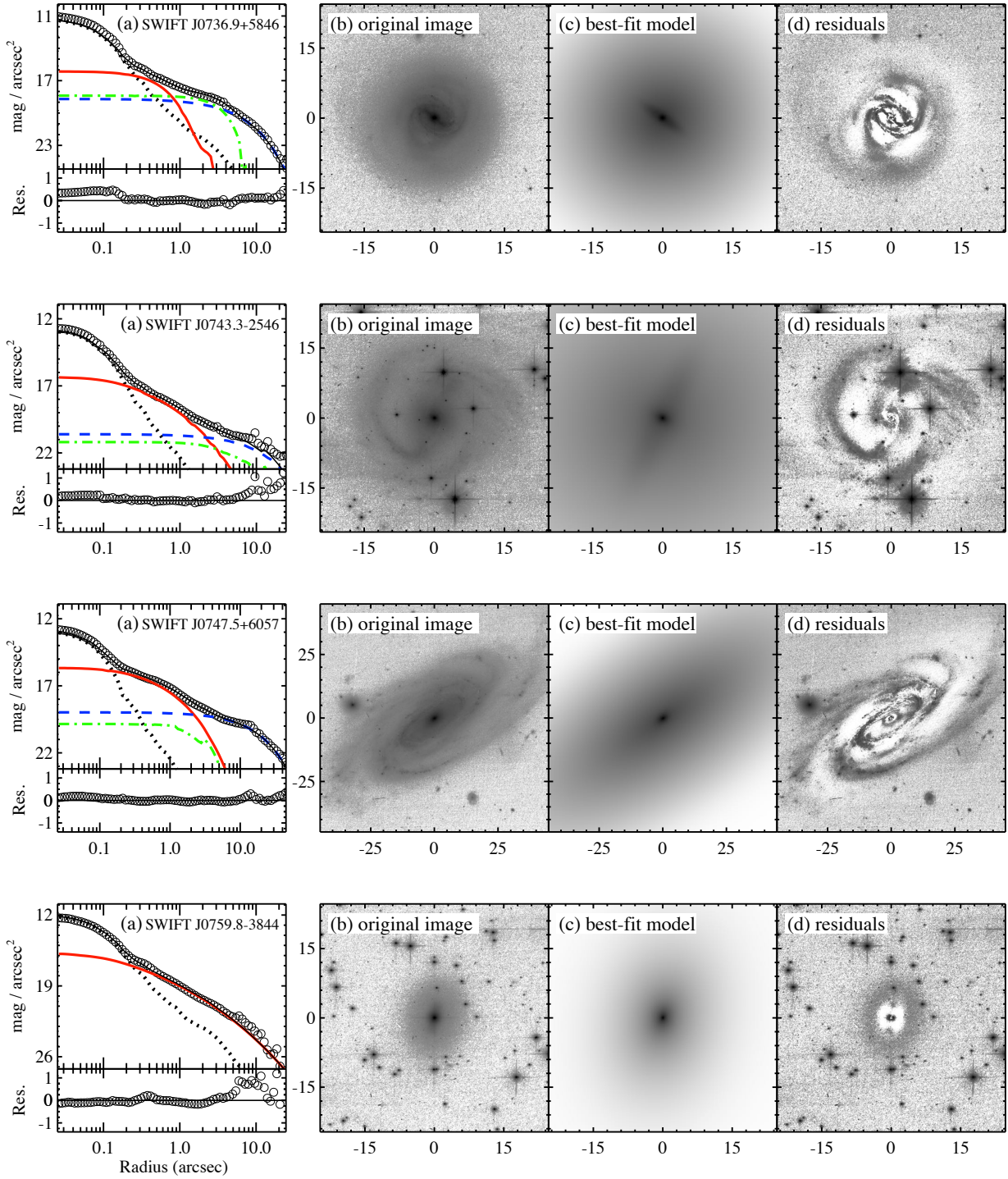


Figure 2. Continued

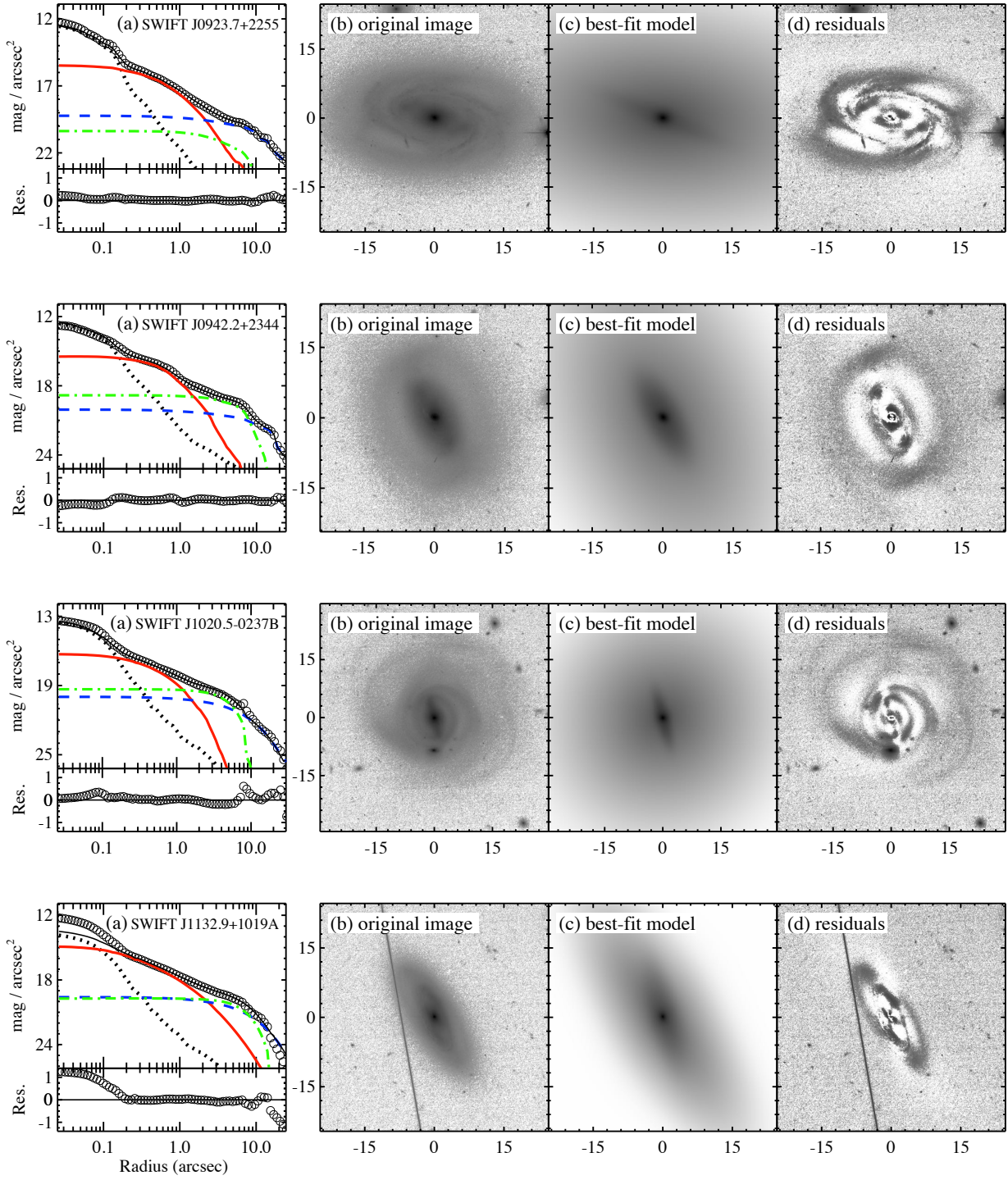


Figure 2. Continued

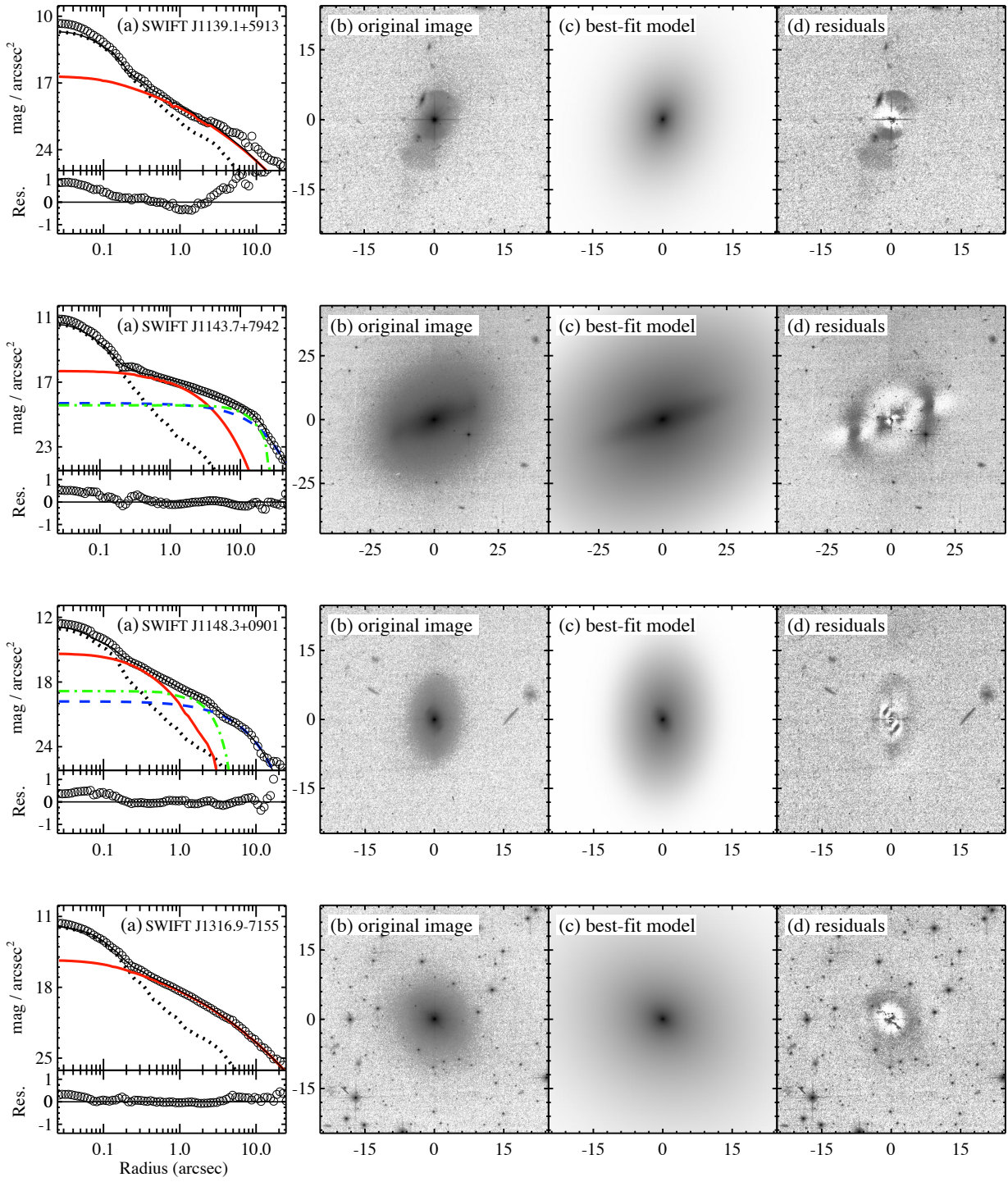


Figure 2. Continued

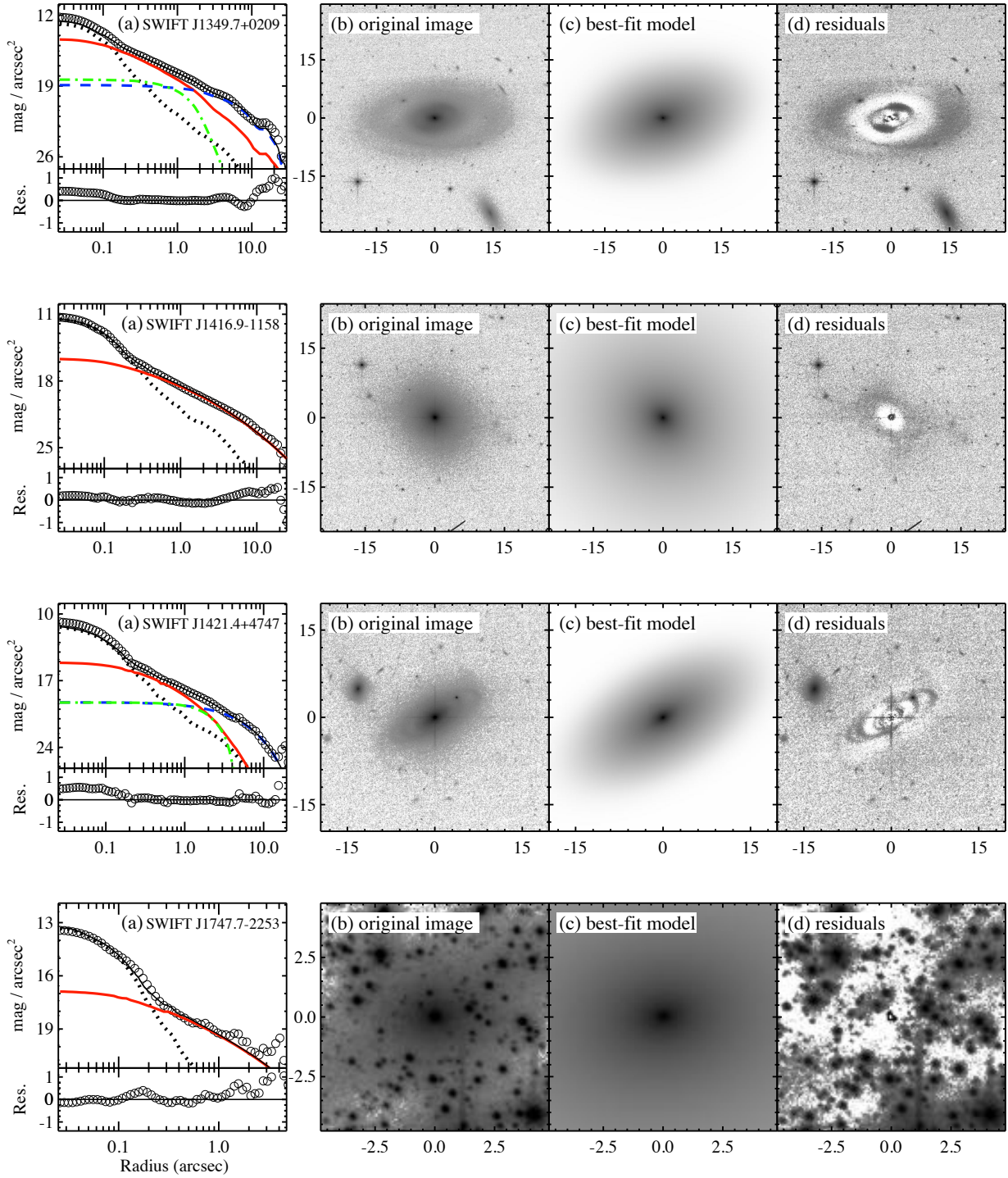


Figure 2. Continued

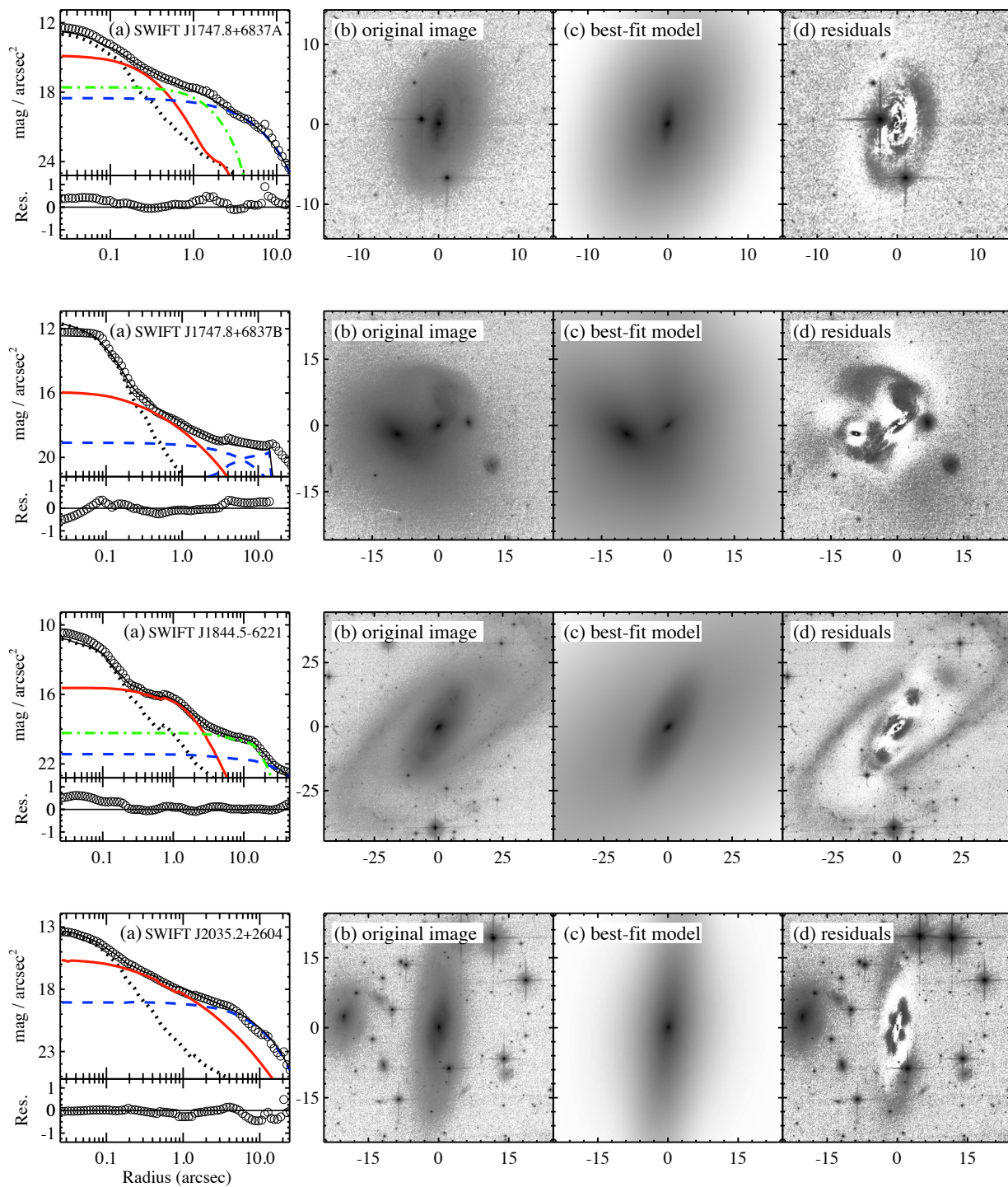


Figure 2. Continued

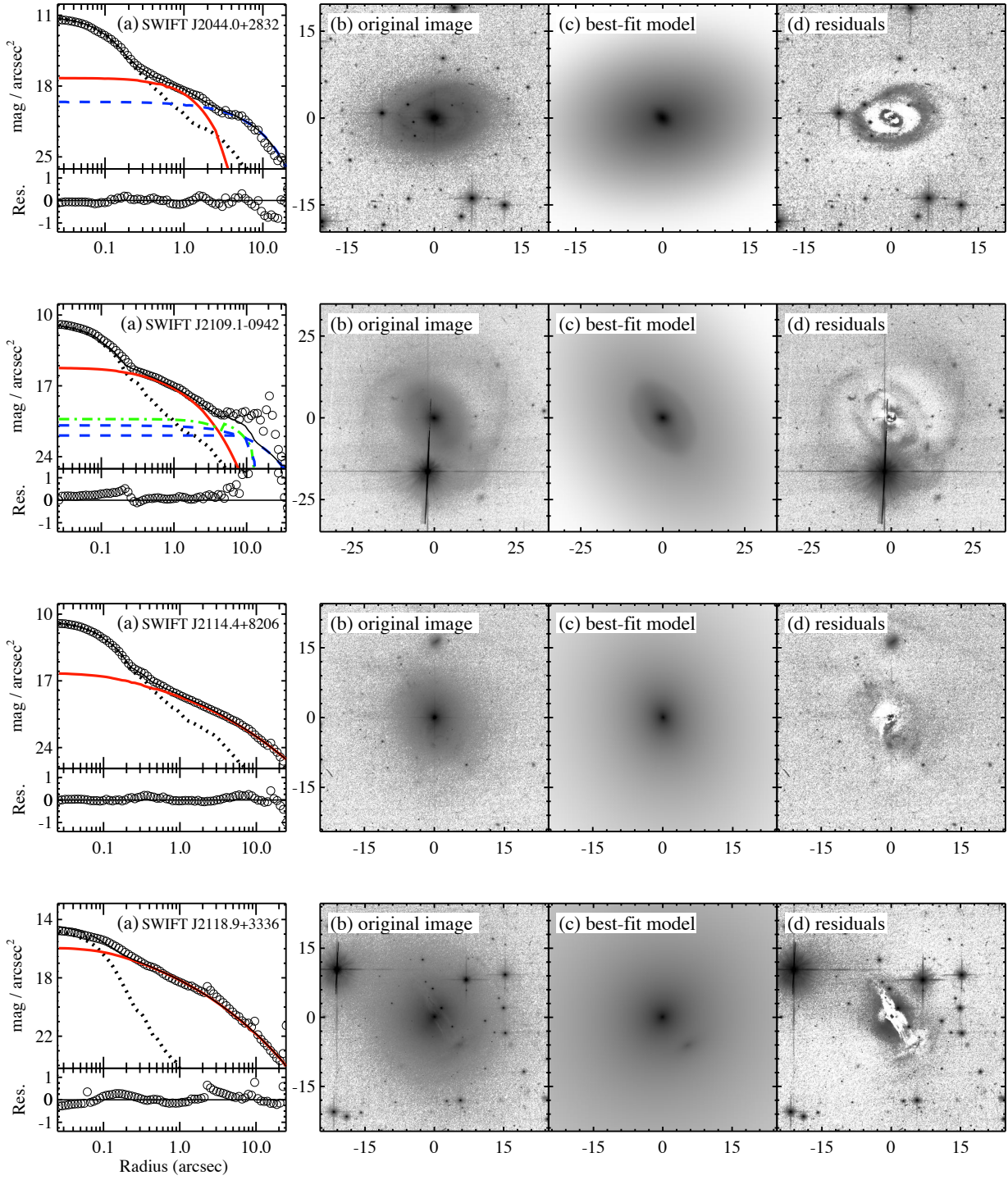


Figure 2. Continued

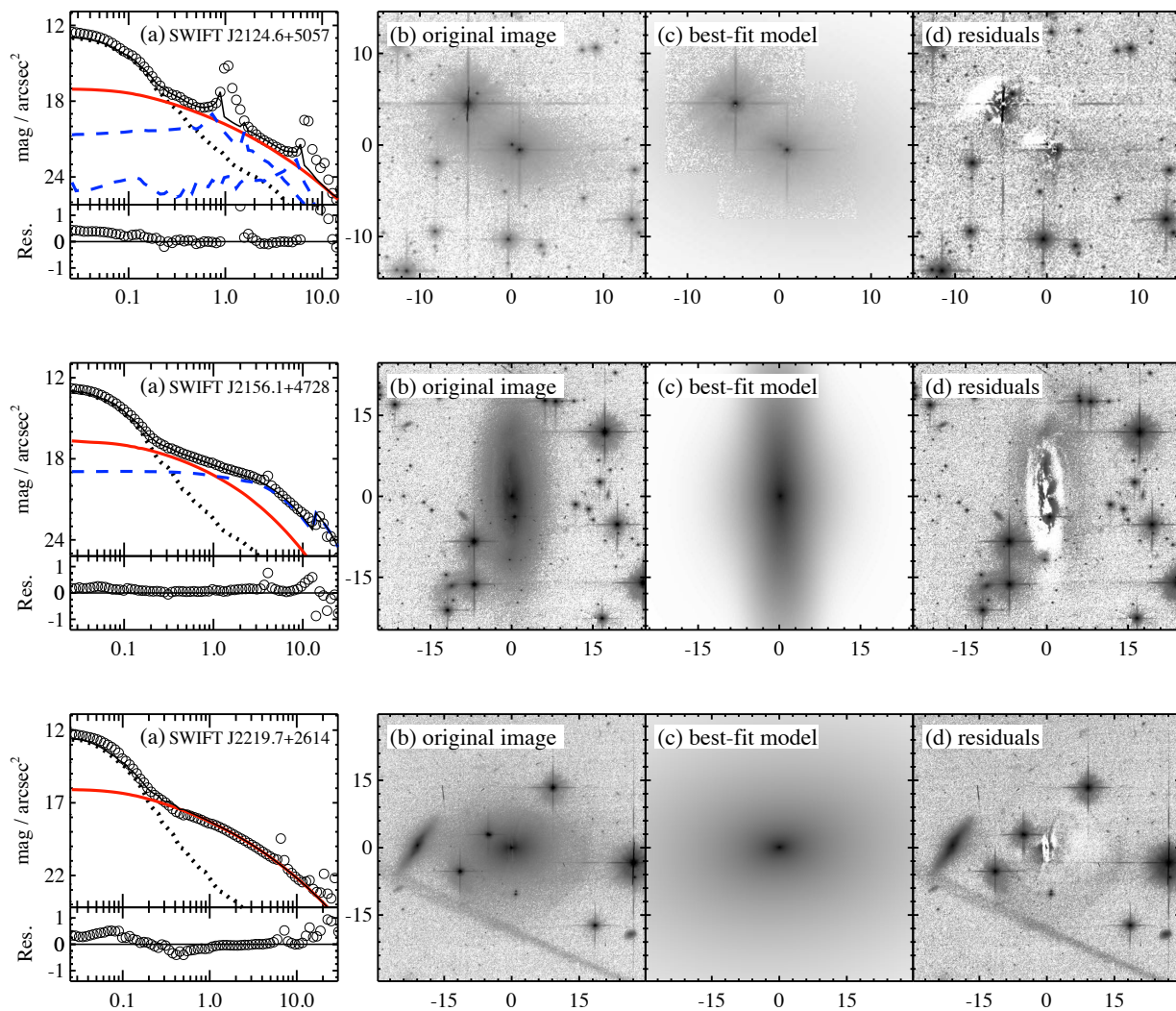


Figure 2. Continued

tion of the *HST* images using GALFIT (Peng et al. 2002, 2010). Before conducting the fit, we manually masked neighboring objects and charge-bleeding trails due to saturation. For robust measurements, it is necessary to adequately model non-bulge components, such as the nucleus, disk, bar, and oval if present along with the bulge component. We employed the empirical PSF to approximate the nucleus. The sub-components of the host galaxies were modeled with Sérsic profiles. As an initial test, we fitted the host galaxy with a single Sérsic profile, where we either fixed the Sérsic index (n) as 1 or 4, or let it float as a free parameter. If there is no clear evidence of additional components (e.g., disk or bar) in the residual images, we conclude that the host is well fitted with the single Sérsic component (i.e., elliptical). For a sanity check for the goodness of the fit, we also utilized 1D surface brightness profiles of the original images and best models and their residuals (Fig. 2).

If any structures other than the bulge are revealed in the residual images, we refit the imaging data by adding Sérsic components: a Sérsic component with $n = 1$ for an exponential disk, a Sérsic component with $n = 0.5$ for a bar, and a Sérsic component with free n for an oval. If the fitting result is severely affected by the light from companion objects, we simultaneously fit them with Sérsic profiles for extended sources or PSFs for point sources. Finally, Fourier modes were additionally implemented to account for the lopsidedness of the host if the host galaxy is heavily disturbed. The detailed fitting results, including 1D surface brightness profiles, are displayed in Figure 2.

Owing to the bright nucleus and PSF mismatch, it is occasionally difficult to choose the best model for the host galaxy from the decomposition with GALFIT. In that case, the fitting result with the most physically meaningful parameters and a smaller reduced χ^2 value was selected as the best fit. For example, Sérsic models with a large Sérsic index ($n > 8$) or a tiny effective radius ($R_e \leq$ a few pixels) were not considered as reliable.

To estimate the uncertainty of the bulge luminosity, we adopted the recipe proposed by Kim et al. (2017) based on imaging simulations. The uncertainty of the bulge luminosity was initially determined by the bulge-to-nucleus light ratio (0.3 mag for $L_{\text{bul}}/L_{\text{nuc}} \geq 0.2$ and 0.4 mag for $L_{\text{bul}}/L_{\text{nuc}} < 0.2$). Then, an additional component (e.g., disk) for the host would increase the uncertainty by 0.1 mag. Additional uncertainty can be introduced from imperfect sky subtraction, which was done as part of the drizzling process. Because the field of view is sufficiently large for robust sky determination, the measurement error for the sky estimation is expected to be small. Nevertheless, to quantify the effect of sky uncertainty, we perform the decomposition by fixing the sky to 1σ and -1σ of the original sky value. This experiment often resulted in host components with unreliable structural parameters (e.g., extremely small or large Sérsic indices with large effective radii), but the impact on the bulge luminosity is modest, usually only within 0.2 mag. Note that PSF mismatch appears to be severe in a few targets (e.g., SWIFT J0123.9–5846,

SWIFT J1132.9+1019A). However, because the bulges are large and bright, as shown in the radial profiles, the total bulge luminosity is only affected at the level of $\sim 0.2 - 0.3$ mag. In addition, such PSF mismatch was taken into account when estimating the error budget (Kim et al. 2017).

We applied a correction for Galactic extinction (Schlafly & Finkbeiner 2011). We performed k -correction using the method in Chilingarian et al. (2010) and Chilingarian & Zolotukhin (2012). The color information of host galaxies is unknown. As a result, we adopt $V - I_C$ color inferred from the morphological types of hosts (Fukugita et al. 1995), which are determined from visual inspection. For the nucleus, $V - I_C \sim 0.6$ is calculated from the QSO composite spectrum (Vanden Berk et al. 2001). The conversion of M_{F814W} to M_I was not applied because the conversion factor is known to be negligible (< 0.05 mag; Fukugita et al. 1995, Harris 2018). Table 3 lists the photometric properties of the sample obtained through the imaging decomposition.

4. RESULTS

4.1. $M_{\text{BH}}-M_{I,\text{bul}}$ Relation

To estimate the $M_{\text{BH}}-M_{I,\text{bul}}$ relation for our sample, we employed a χ^2 minimization fit (modified FITEXY) given in Tremaine et al. (2002), which accounts for the measurement errors in both M_{BH} and $M_{I,\text{bul}}$ and intrinsic scatter (ϵ_0). We fit the $M_{\text{BH}}-M_{I,\text{bul}}$ relation of the form

$$\log(M_{\text{BH}}/M_{\odot}) = \alpha M_{I,\text{bul}} + \beta. \quad (1)$$

Given the small sample size, we fixed the slope to $\alpha = -0.57$, which was derived from the inactive galaxies, and only solved for the zero point (β). To compute the $M_{\text{BH}}-M_{I,\text{bul}}$ relation of the inactive galaxies in I -band from that in K -band (Kormendy & Ho 2013), we used mass-to-light-ratio in K - and I -band inferred from $B - V$ color (Into & Portinari 2013).

It appears that the AGNs in our sample tend to have a lower zero point compared to inactive galaxies (Fig. 3). To find the main driver of this offset, we divided the sample into two subgroups: one with a lower Eddington ratio than the median value (0.06) and one with a higher Eddington ratio than the median value. We find that AGNs with larger Eddington ratio systematically lie below those with smaller Eddington ratio in the $M_{\text{BH}}-M_{I,\text{bul}}$ relation, indicating that the zero point depends on the Eddington ratio.

However, given the fact that hosts with classical bulges and pseudo-bulges follow a different $M_{\text{BH}}-M_{I,\text{bul}}$ relation (Kormendy & Ho 2013), it is essential to assess this trend by dividing the sample according to the bulge type (Ho & Kim 2014). In this light, we performed the bulge classification based on the Sérsic index (n) and B/T . Following the methods given in Fisher & Drory (2008), Gadotti (2009) and Gao et al. (2020), bulges with $n > 2$ and $B/T > 0.2$ ($n \leq 2$ or $B/T \leq 0.2$) are

classified as a classical bulge (pseudo-bulge). Furthermore, we computed the $M_{\text{BH}}-M_{I,\text{bul}}$ relation of inactive galaxies for different bulge types utilizing the data from Kormendy & Ho (2013). The $M_{\text{BH}}-M_{I,\text{bul}}$ relation of the pseudo-bulges has a substantially larger scatter ($\epsilon_0 \sim 0.63$ dex for the pseudo-bulge in inactive galaxies) compared to the classical bulges ($\epsilon_0 \sim 0.31$ dex), which can introduce a systematic bias in the comparison between the two bulge types (Tab. 4). Therefore, classical bulges and ellipticals are considered only for further analysis. By fixing the slope to that of classical bulges and ellipticals in inactive galaxies (~ -0.49), we again find that AGNs with classical bulges or ellipticals lie systematically below the relation of inactive galaxies and the zero point offset is lower for objects with greater Eddington ratio. This observation confirms our previous finding for the entire sample, that the zero point depends on the Eddington ratio.

4.2. Kormendy Relation

There is an anti-correlation between the effective radius (R_e) and the mean surface brightness ($\langle\mu_e\rangle$) within the effective radius, known as the Kormendy relation (Kormendy 1977). Here, we present the Kormendy relation for our sample. Fisher & Drory (2008), Gadotti (2009), and Gao et al. (2020) reported that classical bulges and pseudo-bulges are distinctive in the Kormendy relation, while classical bulges follow the Kormendy relation similar to that of ellipticals. Therefore, we investigated the Kormendy relations as a function of bulge type. We fit the Kormendy relation of the form

$$\langle\mu_e\rangle = \kappa \log(R_e/\text{kpc}) + \gamma, \quad (2)$$

where $\langle\mu_e\rangle$ is the I -band mean surface brightness in the units of mag arcsec^{-2} . We adopted the ordinary least squares bisector method for the fit as both parameters are independent (Isobe et al. 1990).

The Kormendy relation of inactive galaxies in the I band is inferred from that in R band given in Kim & Ho (2019). This process is done by assuming $R - I = 0.65$ for ellipticals and classical bulges, which is equivalent to the value for a galaxy of Hubble type Sab, and $R - I = 0.57$ for pseudo-bulges, which is equivalent to the value for an Scd spiral (Fukugita et al. 1995). For the comparison, we also adopted the Kormendy relation of inactive ellipticals in the I band. It was converted from that in R band from Gao et al. (2020) by assuming $R - I = 0.70$ of an elliptical galaxy (Fukugita et al. 1995). Figure 4 shows that, for ellipticals and classical bulges, there is little difference between the AGNs in our sample and those in inactive galaxies. However, for pseudo-bulges, the AGNs in our sample appear to systematically have brighter $\langle\mu_e\rangle$ compared to those in inactive galaxies at a given R_e . In both types, we found no evidence for a dependence of the Kormendy relation on Eddington ratio. The detailed fitting results for different subsamples are summarized in Table 5.

5. DISCUSSION

5.1. Origin of the Offset in the $M_{\text{BH}}-M_{I,\text{bul}}$ Relation

We find that AGNs in our sample have a lower zero point compared to the inactive galaxies. Additionally, the magnitude of the offset in the zero point ($0.4 - 0.8$ dex) is anti-correlated with the Eddington ratio. This finding can be interpreted in three ways. For AGNs with a high Eddington ratio, either the bulges are over-luminous compared to those in inactive galaxies, the BHs are less massive than those in inactive galaxies at a given bulge luminosity, or BH masses are somehow underestimated. In contrast, ellipticals and classical bulges in our sample follow the Kormendy relation similar to that in inactive galaxies, thereby revealing that there is no excess in the bulge luminosity. Therefore, the offset in the $M_{\text{BH}}-M_{I,\text{bul}}$ relation is unlikely to occur due to the overluminous bulge.

As a BH is actively growing during the AGN phase, it can be naturally expected that AGNs can systematically have less massive BHs than inactive galaxies at a given bulge luminosity. Assuming a constant Eddington ratio within the AGN lifetime (t_{AGN}), a BH growth factor ($\frac{M_{\text{final}}}{M_{\text{int}}}$) during the AGN phase can be expressed as

$$\frac{M_{\text{final}}}{M_{\text{int}}} \approx \exp\left(\lambda \frac{1 - \eta}{\eta} \frac{t_{\text{AGN}}}{t_{\text{Edd}}}\right), \quad (3)$$

where M_{final} is the final BH mass after the AGN phase, M_{int} is the initial BH mass, η is the radiative efficiency of the accretion disk and t_{Edd} is the Eddington time scale (≈ 0.45 Gyr; Volonteri & Rees 2005). For simplicity, we assume $\eta \sim 0.1$ and $t_{\text{AGN}} \sim 0.05$ Gyr (Yu & Tremaine 2002; Martini et al. 2004; Kim & Ho 2019). By adopting the median Eddington ratio of our sample ($\lambda_E \sim 0.06$), the BH growth factor during the AGN phase (~ 1.06 or 0.03 dex) is almost negligible compared to the offset (~ 0.4 dex) in the $M_{\text{BH}}-M_{I,\text{bul}}$ relation. Even with an extreme assumption ($\eta \sim 0.01$; e.g., Davis & Laor 2011), the BH growth factor is less than 0.3 dex. This reveals that undermassive BHs are unlikely to be the main driver of the offset.

It has long been suggested that the scaling factor in the virial mass estimator for BHs can be sensitive to physical properties of AGNs (e.g., Eddington ratio, bolometric luminosity and inclination of BLR; Marconi et al. 2008; Ho & Kim 2014; Mejía-Restrepo et al. 2017). Therefore, the dependence of the zero point offset on the Eddington ratio can be naturally attributed to the different scaling factors instead of a single universal value. To assess this effect more quantitatively, we calculated ΔM_{BH} in each object, which is defined as the offset between the BH mass estimated from the virial method and that inferred from the inactive $M_{\text{BH}}-M_{I,\text{bul}}$ relation at a given bulge luminosity in a log-log space. Then we compared ΔM_{BH} with the Eddington ratio (Fig. 5). The Spearman correlation coefficient is -0.49 (p -value ~ 0.003), which implies that the correlation between two variables is significant. To validate the statistical

significance of the correlation, we employed the bootstrapping resampling method. From this experiment, we found a 68% confidence interval of -0.45 to -0.64 , again indicating that the correlation is statistically significant. Additionally, ΔM_{BH} appears to converge to 0 when the Eddington ratio is smaller than 0.05, which supports the idea that the zero point offset is due to the dependence of the scaling factor on the Eddington ratio. One may argue that the secondary parameter (e.g., M_{BH}) can be another origin of the systematic offset. To test this hypothesis, we computed the Spearman correlation coefficient (~ 0.41 with p -value ~ 0.02) between ΔM_{BH} and M_{BH} . Although the coefficient value is slightly smaller than that of the correlation between ΔM_{BH} and the Eddington ratio, it appears to be moderate. We perform a partial correlation analysis to further investigate whether Eddington ratio or M_{BH} is the primary parameter driving the zero point offset. We find a higher partial correlation coefficient ($\rho \sim -0.38$) between ΔM_{BH} and Eddington ratio after removing the contribution from BH mass. Note that the coefficient between ΔM_{BH} and BH mass excluding the effect from Eddington ratio is -0.13 . Therefore, we conclude that Eddington ratio is likely to be a main driver of the zero point offset. The last caveat is that low-mass AGNs ($M_{\text{BH}} \leq 10^{7.5} M_{\odot}$) with a low Eddington ratio may be excluded with the flux-limited hard X-ray selection. This may be a possible scenario to explain the observed zero point offset, but we cannot address it in this study given the small sample size.

5.2. Comparison with Previous Studies

Previous studies with *HST* imaging dataset of nearby type 1 AGNs also utilized the BH–host and Kormendy relations to investigate the physical connection between SMBHs and host galaxies of AGNs (e.g., Kim et al. 2008b; Kim & Ho 2019; Zhao et al. 2019, 2021). However, they reached somewhat different conclusions. For example, Kim & Ho (2019) found that AGNs lie systematically below in the $M_{\text{BH}}-M_{R,\text{bul}}$ relation compared to normal galaxies, and they concluded that bulges hosting AGNs are overluminous possibly due to the young stellar population based on the archival data of nearby AGNs ($z < 0.35$). Those observational results are in broad agreement with our finding in the sense that AGNs are offset from the normal galaxies in the $M_{\text{BH}}-M_{\text{bul}}$ relation. However, their interpretation is somewhat different from ours, possibly because they partly used B - and V -band magnitudes that are more sensitive to young stellar populations compared to I -band used in this study. Additionally, unlike our sample, the sample in Kim & Ho (2019) is somewhat heterogeneous, and the archival imaging data were obtained in various observing configurations (e.g., instrument, filter, and exposure time). Therefore, their result can suffer from hidden biases.

In contrast, Zhao et al. (2021) reported that AGNs with massive hosts follow scaling relations ($M_{\text{BH}}-M_{*,\text{bul}}$ and Kormendy relation) similar to those of normal galaxies, based on color images of PG quasars ($z < 0.5$).

These results are inconsistent with our finding that ellipticals and classical bulges hosting AGNs deviate from the $M_{\text{BH}}-M_{I,\text{bul}}$ relation of those in normal galaxies. The massive AGNs in Zhao et al. (2021) are more distant ($z \sim 0.4$) than those in our sample ($z < 0.1$), and may be affected by cosmic evolution and/or unknown bias. They also found that only the late-type galaxies with pseudo-bulges of AGNs deviate in the scaling relations, indicating that the brightness of pseudo-bulges hosting AGNs is enhanced due to recent star formation (e.g., Zhuang & Ho 2020; Xie et al. 2021; Zhuang et al. 2021). Interestingly, we also find the same offset in the Kormendy relation only for pseudo-bulges.

6. CONCLUSION

In this paper, we estimated the photometric properties of the bulges in the host galaxies by performing the careful imaging decomposition on *HST* images of 35 nearby AGNs, originally selected from hard X-ray data. Along with BH mass estimates from the virial methods, we examined the $M_{\text{BH}}-M_{I,\text{bul}}$ and Kormendy relations of our sample and compared them with those of inactive galaxies. The main results from these experiments can be summarized as follows.

- The $M_{\text{BH}}-M_{I,\text{bul}}$ relation of our sample AGNs slightly deviate from that of inactive galaxies in the sense that the BH mass in our sample AGNs is ~ 0.4 dex less than that of inactive galaxies at a given bulge luminosity. The zero point offset in the $M_{\text{BH}}-M_{I,\text{bul}}$ relation of elliptical and classical bulges in our sample compared to that in inactive galaxies appears to be correlated with the Eddington ratio.
- For ellipticals and classical bulges, our sample follows the Kormendy relation in a similar manner as normal galaxies, indicating there is no evidence for overluminous bulges in our sample. As a result, we conclude that the zero point offset is possibly due to the dependence of the scaling factor on the Eddington ratio.
- Pseudo-bulges in our sample AGNs tend to be overluminous compared to those in normal galaxies, which is inferred from the Kormendy relation. This property of the pseudo-bulges is possibly due to the young stellar populations in the AGN host.

ACKNOWLEDGMENTS

We thank the anonymous referee for the constructive feedback that helped to improve the quality of the paper. This work is based on observations made with the NASA/ESA Hubble Space Telescope, obtained at the Space Telescope Science Institute, which is operated by the Association of Universities for Research in Astronomy, Inc., under NASA contract NAS5-26555. These observations are associated with program #15444. LCH was supported by the National Science Foundation of China (11721303, 11991052,

12011540375).), China Manned Space Project (CMS-CSST-2021-A04), and the National Key R&D Program of China (2016YFA0400702). This work was supported by a National Research Foundation of Korea (NRF) grant (No. 2020R1A2C4001753) funded by the Korean government (MSIT) and under the framework of international cooperation program managed by the National Research Foundation of Korea (NRF-2020K2A9A2A06026245). This research made use of the “*k*-corrections calculator” service available at <http://kcor.sai.msu.ru/>.

REFERENCES

- Bennert, V. N., Treu, T., Woo, J.-H., et al. 2010, Cosmic Evolution of Black Holes and Spheroids. IV. The $M_{\text{BH}} - L_{\text{sph}}$ Relation, *ApJ*, 708, 1507
- Bentz, M. C., Denney, K. D., Grier, C. J., et al. 2013, The Low-luminosity End of the Radius–Luminosity Relationship for Active Galactic Nuclei, *ApJ*, 767, 149
- Chilingarian, I., Melchior, A.-L., & Zolotukhin, I. 2010, Analytical Approximations of *K*-corrections in Optical and Near-infrared Bands, *MNRAS*, 405, 1409
- Chilingarian, I. & Zolotukhin, I. 2012, A Universal Ultraviolet-optical Colour–colour–magnitude Relation of Galaxies, *MNRAS*, 419, 1727
- Davis, S.W. & Laor A. 2011 The Radiative Efficiency of Accretion Flows in Individual Active Galactic Nuclei, *ApJ*, 728, 98
- Di Matteo, T., Springel, V., & Hernquist, L. 2005, Energy Input from Quasars Regulates the Growth and Activity of Black Holes and Their Host Galaxies, *Nature*, 433, 604
- Du, P., Lu, K.-X., Zhang, Z.-X., et al. 2016, Supermassive Black Holes with High Accretion Rates in Active Galactic Nuclei. V. A New Size-Luminosity Scaling Relation for the Broad-line Region, *ApJ*, 825, 126
- Fisher, D. B. & Drory, N. 2008, The Structure of Classical Bulges and Pseudobulges: the Link Between Pseudobulges and Sérsic Index, *AJ*, 136, 773
- Fonseca Alvarez, G. F., Trump, J. R., Homayouni, Y., et al. 2020, The Sloan Digital Sky Survey Reverberation Mapping Project: The $H\beta$ Radius–Luminosity Relation, *ApJ*, 899, 73
- Fukugita, M., Shimasaku, K., & Ichikawa, T. 1995, Galaxy Colors in Various Photometric Band Systems, *PASP*, 107, 945
- Gadotti, D. A. 2009 Structural Properties of Pseudo-bulges, Classical bulges and Elliptical galaxies: a Sloan Digital Sky Survey Perspective, *MNRAS*, 393, 1531
- Gao, H., Ho, L. C., Barth, A. J., & Li, Z.-Y. 2020, The Carnegie-Irvine Galaxy Survey. IX. Classification of Bulge Types and Statistical Properties of Pseudo Bulges, *ApJS*, 247, 20
- Greene, J. E. & Ho, L. C. 2005, Estimating Black Hole Masses in Active Galaxies Using the $H\alpha$ Emission Line, *ApJ*, 630, 122
- Grogin, N. A., Lim, P. L., Maybhate, et al. 2010, Post-SM4 ACS/WFC Bias Stripping: Characterization And Mitigation, The 2010 HST Calibration Workshop, ed. S. Deustua & C. Oliveira (Baltimore, MD: STScI), 54
- Harris, W. E. 2018, Transformation of HST WFC3/UVIS Filters to the Standard BVI System, *AJ*, 156, 296
- Ho, L. C. 2008, Nuclear Activity in Nearby Galaxies, *ARA&A*, 46, 475
- Ho, L. C. & Kim, M. 2014, The Black Hole Mass Scale of Classical and Pseudo Bulges in Active Galaxies, *ApJ*, 789, 17
- Ho, L. C. & Kim, M. 2015, A Revised Calibration of the Virial Mass Estimator for Black Holes in Active Galaxies Based on Single-epoch $H\beta$ Spectra, *ApJ*, 809, 123
- Into, T. & Portinari, L. 2013, New Colour–mass-to-light relations: the Role of the Asymptotic Giant Branch Phase and of Interstellar Dust, *MNRAS*, 430, 2715
- Isobe, T., Feigelson, E. D., Akritas, M. G., & Babu, G. J. 1990, Linear Regression in Astronomy. I., *ApJ*, 364, 104
- Kaspi, S., Smith, P. S., Netzer, H., et al. 2000, Reverberation Measurements for 17 Quasars and the Size-Mass-Luminosity Relations in Active Galactic Nuclei, *ApJ*, 533, 631
- Kim, M., Barth, A. J., Ho, L. C., et al. 2021, A Hubble Space Telescope Imaging Survey of Low-redshift Swift-BAT Active Galaxies, *ApJS*, 256, 40
- Kim, M., & Ho, L. C. 2019, Evidence for a Young Stellar Population in Nearby Type 1 Active Galaxies, *ApJ*, 876, 35
- Kim, M., Ho, L. C., Peng, C. Y., et al. 2008a, Decomposition of the Host Galaxies of Active Galactic Nuclei Using Hubble Space Telescope Images, *ApJS*, 179, 283
- Kim, M., Ho, L. C., Peng, C. Y., et al. 2008b, The Origin of the Intrinsic Scatter in the Relation Between Black Hole Mass and Bulge Luminosity for Nearby Active Galaxies, *ApJ*, 687, 767
- Kim, M., Ho, L. C., Peng, C. Y., et al. 2017, Stellar Photometric Structures of the Host Galaxies of Nearby Type 1 Active Galactic Nuclei, *ApJS*, 232, 21
- Kormendy, J. 1977, Brightness Distributions in Compact and Normal Galaxies. II. Structure Parameters of the Spheroidal Component, *ApJ*, 218, 333
- Kormendy, J., Ho, L. C. 2013, Coevolution (Or Not) of Supermassive Black Holes and Host Galaxies, *ARA&A*, 51, 511
- Koss, M., Trakhtenbrot, B., Ricci, C., et al. 2017, BAT AGN Spectroscopic Survey. I. Spectral Measurements, Derived Quantities, and AGN Demographics, *ApJ*, 850, 74
- Krist, J. E., Hook, R. N., & Stoehr, F. 2011, 20 years of Hubble Space Telescope Optical Modeling Using Tiny Tim, *Proc. SPIE*, 8127, 81270J
- Lyke, B. W., Higley, A. N., McLane, J. N., et al. 2020, The Sloan Digital Sky Survey Quasar Catalog: Sixteenth Data Release, *ApJS*, 250, 8
- Marconi, A., Axon, D. J., Maiolino, R., et al. 2008, The Effect of Radiation Pressure on Virial Black Hole Mass Estimates and the Case of Narrow-Line Seyfert 1 Galaxies, *ApJ*, 678, 693
- Martini, P. 2004, Why Does Low-Luminosity AGN Fueling Remain an Unsolved Problem?, in *IAU Symp. 222, The Interplay Among Black Holes, Stars and ISM in Galactic Nuclei*, ed. T. Storchi-Bergmann, L. C. Ho, & H. R. Schmitt (Cambridge: Cambridge Univ. Press), 235
- Mejía-Restrepo, J. E., Lira, P., Netzer, H., et al. 2017, The Virial Factor and Biases in Single Epoch Black Hole Mass Determinations, *Front. Astron. Space Sci.*, 4, 70
- Park, D., Woo, J.-H., Bennert, V. N., et al. 2014, Cosmic Evolution of Black Holes and Spheroids. V. The Relation between Black Hole Mass and Host Galaxy Luminosity for a Sample of 79 Active Galaxies *ApJ*, 799, 164
- Peng, C. Y., Ho, L. C., Impey, C. D., & Rix, H.-W. 2002, Detailed Structural Decomposition of Galaxy Images, *AJ*, 124, 266

Table 1
The Sample.

Source Name	Alternative Name	Exposure (s)	R.A. (deg.)	Dec. (deg.)	A_{F814W} (mag)	z	D_{L} (Mpc)
(1)	(2)	(3)	(4)	(5)	(6)	(7)	(8)
SWIFT J0123.9-5846	Fairall 9	674	20.9408	-58.8057	0.039	0.0460	210.4
SWIFT J0157.2+4715	2MASX J01571097+4715588	674	29.2956	47.2666	0.228	0.0478	218.9
SWIFT J0206.2-0019	Mrk 1018	674	31.5666	-0.2914	0.042	0.0430	196.2
SWIFT J0234.6-0848	NGC 985	674	38.6574	-8.7876	0.050	0.0430	196.4
SWIFT J0333.3+3720	2MASX J03331873+3718107	674	53.3282	37.3030	0.815	0.0547	251.8
SWIFT J0429.6-2114	2MASX J04293830-2109441	674	67.4095	-21.1622	0.037	0.0700	325.8
SWIFT J0510.7+1629	IRAS 05078+1626	674	77.6896	16.4989	0.457	0.0173	77.7
SWIFT J0516.2-0009	Ark 120	674	79.0476	-0.1498	0.194	0.0325	147.1
SWIFT J0736.9+5846	Mrk 9	674	114.2374	58.7704	0.089	0.0398	181.5
SWIFT J0743.3-2546	LEDA 86073	674	115.8114	-25.7639	1.096	0.0238	106.5
SWIFT J0747.5+6057	Mrk 10	554	116.8714	60.9335	0.071	0.0294	131.6
SWIFT J0759.8-3844	2MASX J07594181-3843560	674	119.9242	-38.7322	1.238	0.0402	183.2
SWIFT J0923.7+2255	MCG +04-22-042	674	140.9292	22.9090	0.067	0.0333	150.8
SWIFT J0942.2+2344	CGCG 122-055	674	145.5200	23.6853	0.038	0.0217	97.4
SWIFT J1020.5-0237B	2MASX J10195855-0234363	674	154.9941	-2.5767	0.062	0.0595	274.7
SWIFT J1132.9+1019A	IC 2921	674	173.2053	10.2965	0.050	0.0440	201.0
SWIFT J1139.1+5913	SBS 1136+594	674	174.7870	59.1990	0.023	0.0616	284.8
SWIFT J1143.7+7942	UGC 06728	674	176.3168	79.6815	0.155	0.0063	28.1
SWIFT J1148.3+0901	2MASX J11475508+0902284	674	176.9795	9.0413	0.041	0.0693	322.2
SWIFT J1316.9-7155	2MASX J13165424-7155270	674	199.2262	-71.9242	0.389	0.0703	327.2
SWIFT J1349.7+0209	UM 614	674	207.4701	2.0791	0.043	0.0331	150.0
SWIFT J1416.9-1158	2MASX J14165001-1158577	674	214.2084	-11.9829	0.102	0.0992	471.1
SWIFT J1421.4+4747	SBS 1419+480	674	215.3742	47.7902	0.027	0.0727	338.8
SWIFT J1747.7-2253	2MASX J17472972-2252448	674	266.8739	-22.8791	1.555	0.0467	213.9
SWIFT J1747.8+6837A	Mrk 507	674	267.1599	68.7044	0.059	0.0551	253.9
SWIFT J1747.8+6837B	VII Zw 742	674	266.7493	68.6102	0.057	0.0630	291.5
SWIFT J1844.5-6221	Fairall 51	674	281.2249	-62.3648	0.165	0.0140	62.3
SWIFT J2035.2+2604	2MASX J20350566+2603301	674	308.7735	26.0583	0.415	0.0478	218.9
SWIFT J2044.0+2832	RX J2044.0+2833	674	311.0188	28.5534	0.524	0.0489	224.0
SWIFT J2109.1-0942	2MASX J21090996-0940147	674	317.2915	-9.6707	0.325	0.0267	120.7
SWIFT J2114.4+8206	2MASX J21140128+8204483	674	318.5049	82.0801	0.233	0.0833	391.0
SWIFT J2118.9+3336	2MASX J21192912+3332566	674	319.8714	33.5491	0.328	0.0509	233.7
SWIFT J2124.6+5057	4C 50.55	674	321.1643	50.9735	3.709	0.0151	67.4
SWIFT J2156.1+4728	2MASX J21355399+4728217	674	323.9750	47.4727	0.969	0.0253	114.0
SWIFT J2219.7+2614	2MASX J22194971+2613277	674	334.9573	26.2244	0.165	0.0877	413.2

Col. (1): Source name. Col. (2): Alternative name. Col. (3): Exposure time. Col. (4): Right Ascension. Col. (5): Declination. Col. (6): Galactic extinction in F814W. Col. (7): Redshift. Col. (8): Luminosity distance.

Table 2
Physical Properties of the Sample.

Source Name	Line	Bulge Type	$\log M_{\text{BH}}$ (M_{\odot})	$\log L_{\text{bol}}$ (erg s^{-1})	$\log \lambda_{\text{E}}$
(1)	(2)	(3)	(4)	(5)	(6)
SWIFT J0123.9–5846	H α	PB	8.07	45.32	–0.85
SWIFT J0157.2+4715	H α	PB	7.54	44.84	–0.80
SWIFT J0206.2–0019	H α	E	8.11	45.01	–1.20
SWIFT J0234.6–0848	H α	PB	8.13	45.02	–1.21
SWIFT J0333.3+3720	H α	E	8.25	45.14	–1.21
SWIFT J0429.6–2114	H α	E	8.83	45.00	–1.93
SWIFT J0510.7+1629	H α	E	7.76	44.72	–1.14
SWIFT J0516.2–0009	H α	CB	8.78	45.11	–1.77
SWIFT J0736.9+5846	H α	PB	7.53	44.40	–1.23
SWIFT J0743.3–2546	H α	PB	7.09	44.30	–0.89
SWIFT J0747.5+6057	H α	PB	7.24	44.36	–0.98
SWIFT J0759.8–3844	H α	E	8.62	45.15	–1.57
SWIFT J0923.7+2255	H α	PB	7.23	44.87	–0.46
SWIFT J0942.2+2344	H α	PB	7.04	43.98	–1.16
SWIFT J1020.5–0237B	H β	PB	8.29	44.60	–1.79
SWIFT J1132.9+1019A	H α	CB	7.95	44.72	–1.33
SWIFT J1139.1+5913	H α	E	8.31	45.14	–1.27
SWIFT J1143.7+7942	H α	PB	5.71	43.28	–0.53
SWIFT J1148.3+0901	H α	PB	8.33	45.02	–1.41
SWIFT J1316.9–7155	H β	E	9.15	45.16	–2.09
SWIFT J1349.7+0209	H α	CB	7.61	44.51	–1.20
SWIFT J1416.9–1158	H β	E	9.17	45.53	–1.74
SWIFT J1421.4+4747	H α	CB	8.65	45.27	–1.48
SWIFT J1747.7–2253	H α	E	9.09	44.93	–2.26
SWIFT J1747.8+6837A	H α	PB	6.91	44.35	–0.66
SWIFT J1747.8+6837B	H α	PB	6.90	44.59	–0.41
SWIFT J1844.5–6221	H α	PB	6.90	44.15	–0.85
SWIFT J2035.2+2604	H α	CB	7.63	44.67	–1.06
SWIFT J2044.0+2832	H α	PB	7.93	44.93	–1.10
SWIFT J2109.1–0942	H α	PB	7.22	44.40	–0.92
SWIFT J2114.4+8206	H α	E	9.13	45.68	–1.55
SWIFT J2118.9+3336	H α	E	8.22	44.77	–1.55
SWIFT J2124.6+5057	H α	E	6.80	44.95	0.05
SWIFT J2156.1+4728	H α	CB	7.58	44.39	–1.29
SWIFT J2219.7+2614	H α	E	9.12	45.41	–1.81

Col. (1): Source name. Col. (2): Line used to estimate BH mass. Col. (3): Bulge type: "E"=elliptical, "CB"=classical bulge, "PB"=pseudo-bulge. Col. (4): BH mass. Col. (5): Bolometric luminosity inferred from the intrinsic X-ray luminosity (Ricci et al. 2017). Col. (6): Eddington ratio.

Table 3
Photometric Properties of the Sample.

Source Name (1)	Nuclear	Bulge				Host		
	M_I (mag) (2)	M_I (mag) (3)	n (4)	R_e (arcsec) (5)	$\langle\mu_e\rangle$ (mag arcsec $^{-2}$) (6)	M_I (mag) (7)	$L_{\text{bul}}/L_{\text{nuc}}$ (8)	B/T (9)
SWIFT J0123.9-5846	-21.68	-22.00 ± 0.40	0.99	0.61	15.50	-23.77	1.34	0.20
SWIFT J0157.2+4715	-19.42	-21.13 ± 0.40	1.47	0.75	16.80	-22.89	4.83	0.20
SWIFT J0206.2-0019	-19.53	-23.90 ± 0.30	4(f)	8.58	19.33	-23.90	55.94	1.00
SWIFT J0234.6-0848	-21.70	-21.78 ± 0.40	1.48	1.75	18.00	-23.56	1.08	0.19
SWIFT J0333.3+3720	-21.68	-23.02 ± 0.30	4(f)	7.98	20.05	-23.02	3.45	1.00
SWIFT J0429.6-2114	-21.72	-23.62 ± 0.30	4(f)	9.30	19.79	-23.62	5.71	1.00
SWIFT J0510.7+1629	-19.54	-20.96 ± 0.30	4(f)	3.10	20.06	-20.96	3.70	1.00
SWIFT J0516.2-0009	-22.21	-22.96 ± 0.40	4(f)	2.65	17.72	-23.32	1.99	0.72
SWIFT J0736.9+5846	-21.01	-19.99 ± 0.40	0.70	0.38	16.50	-22.86	0.39	0.07
SWIFT J0743.3-2546	-19.34	-20.11 ± 0.40	2.17	0.59	17.30	-22.54	2.04	0.11
SWIFT J0747.5+6057	-18.67	-20.77 ± 0.40	1.50	0.82	17.36	-23.28	6.89	0.10
SWIFT J0759.8-3844	-21.43	-21.83 ± 0.30	4(f)	1.88	18.11	-21.83	1.44	1.00
SWIFT J0923.7+2255	-19.45	-20.91 ± 0.40	1.37	0.66	16.76	-22.77	3.85	0.18
SWIFT J0942.2+2344	-18.45	-19.74 ± 0.40	0.96	0.30	16.19	-21.51	3.28	0.20
SWIFT J1020.5-0237B	-19.76	-21.13 ± 0.40	1.31	0.94	17.30	-23.29	3.52	0.14
SWIFT J1132.9+1019A	-18.77	-21.37 ± 0.40	2.66	0.97	17.14	-22.47	10.99	0.36
SWIFT J1139.1+5913	-21.69	-20.90 ± 0.30	4(f)	2.45	19.61	-20.90	0.48	1.00
SWIFT J1143.7+7942	-16.62	-18.42 ± 0.40	1.35	0.30	17.54	-20.35	5.21	0.17
SWIFT J1148.3+0901	-20.36	-20.97 ± 0.40	1.39	0.50	16.10	-22.37	1.76	0.27
SWIFT J1316.9-7155	-21.98	-23.19 ± 0.30	4(f)	4.17	18.48	-23.19	3.05	1.00
SWIFT J1349.7+0209	-19.08	-20.53 ± 0.40	4(f)	0.57	16.82	-21.68	3.81	0.35
SWIFT J1416.9-1158	-22.94	-23.69 ± 0.30	4(f)	7.31	19.19	-23.69	2.01	1.00
SWIFT J1421.4+4747	-22.34	-21.89 ± 0.40	2.04	1.01	16.68	-22.75	0.66	0.46
SWIFT J1747.7-2253	-20.84	-22.72 ± 0.30	4(f)	5.38	19.50	-22.72	5.67	1.00
SWIFT J1747.8+6837A	-19.95	-20.21 ± 0.40	1.21	0.25	15.31	-22.47	1.27	0.13
SWIFT J1747.8+6837B	-21.71	-21.63 ± 0.40	2.66	2.55	18.97	-23.87	0.92	0.13
SWIFT J1844.5-6221	-18.99	-19.71 ± 0.40	1.23	0.37	16.70	-21.74	1.95	0.15
SWIFT J2035.2+2604	-19.56	-21.78 ± 0.40	3.24	2.18	18.48	-22.73	7.69	0.42
SWIFT J2044.0+2832	-21.95	-20.81 ± 0.40	0.77	0.88	17.47	-22.32	0.35	0.25
SWIFT J2109.1-0942	-20.69	-21.22 ± 0.40	1.47	0.64	16.37	-22.25	1.63	0.39
SWIFT J2114.4+8206	-23.23	-23.57 ± 0.30	4(f)	10.73	20.15	-23.57	1.37	1.00
SWIFT J2118.9+3336	-18.40	-23.67 ± 0.30	4(f)	10.33	19.97	-23.67	127.82	1.00
SWIFT J2124.6+5057	-20.96	-21.33 ± 0.30	4(f)	0.99	17.22	-21.33	1.41	1.00
SWIFT J2156.1+4728	-19.26	-20.29 ± 0.40	2.73	1.11	18.50	-21.73	2.57	0.27
SWIFT J2219.7+2614	-21.45	-24.07 ± 0.30	4(f)	14.93	20.36	-24.07	11.16	1.00

Col. (1): Source name. Col. (2): Absolute I -band luminosity of nucleus. Col. (3): Absolute I -band luminosity of bulge. Col. (4): Sérsic index of bulge; “(f)” implies that n is fixed to 4. Col. (5): Effective radius of bulge. Col. (6): Mean surface brightness within the effective radius. Col. (7): Absolute I -band luminosity of host galaxy. Col. (8): The luminosity ratio of bulge to nucleus. Col. (9): Bulge-to-total light ratio.

Table 4
 $M_{\text{BH}}-M_{I,\text{bul}}$ Relation for Various Subsamples.

Subsamples (1)	α (2)	β (3)	ϵ_0 (4)
Inactive (All)	-0.57	-4.17 ± 0.82	0.53 ± 0.06
AGNs (All)	-0.57	-4.40 ± 0.09	0.23 ± 0.10
AGNs (All; $\lambda_E \leq 0.06$)	-0.57	-4.19 ± 0.10	0.11 ± 0.11
AGNs (All; $\lambda_E > 0.06$)	-0.57	-4.64 ± 0.10	0.12 ± 0.09
Inactive (E+CB)	-0.49	-2.22 ± 0.62	0.31 ± 0.03
AGNs (E+CB)	-0.49	-2.62 ± 0.13	0.28 ± 0.12
AGNs (E+CB; $\lambda_E \leq 0.06$)	-0.49	-2.46 ± 0.11	0.03 ± 0.09
AGNs (E+CB; $\lambda_E > 0.06$)	-0.49	-3.06 ± 0.23	0.38 ± 0.14
Inactive (PB)	-0.49	-2.92 ± 0.14	0.62 ± 0.14
AGNs (PB)	-0.49	-2.74 ± 0.11	0.13 ± 0.11
AGNs (PB; $\lambda_E \leq 0.06$)	-0.49	-2.20 ± 0.10	0.00 ± 0.00
AGNs (PB; $\lambda_E > 0.06$)	-0.49	-2.92 ± 0.10	0.00 ± 0.06

Col. (1): Subsample. Col. (2): Slope. Col. (3): Zero point. Col. (4): Intrinsic scatter.

Table 5
Kormendy Relation for Various Subsamples.

Subsamples (1)	κ (2)	γ (3)
Inactive (E) [G]	2.38 ± 0.07	17.16
Inactive (E+CB)	2.53 ± 0.06	17.66
Inactive (PB)	3.94 ± 0.29	18.94
AGNs (All)	2.56 ± 0.20	17.44
AGNs (E+CB)	2.47 ± 0.33	17.51
AGNs (E+CB; $\lambda_E \leq 0.06$)	2.51 ± 0.40	17.43
AGNs (E+CB; $\lambda_E > 0.06$)	2.57 ± 0.91	17.60
AGNs (PB)	2.52 ± 0.61	17.40
AGNs (PB; $\lambda_E \leq 0.06$)	2.67 ± 0.71	17.31
AGNs (PB; $\lambda_E > 0.06$)	2.53 ± 0.81	17.44

Col. (1): Subsample; “[G]” denotes that the subsample comes from Gao et al. (2020). Col. (2): Slope. Col. (3): Zero point.

- Peng, C. Y., Ho, L. C., Impey, C. D., & Rix, H.-W. 2010, Detailed Decomposition of Galaxy Images. II. Beyond Axisymmetric Models, *AJ*, 139, 2097
- Peng, C. Y., Impey, C. D., & Rix, H.-W., et al. 2006, Probing the Coevolution of Supermassive Black Holes and Galaxies Using Gravitationally Lensed Quasar Hosts, *ApJ*, 649, 616
- Planck Collaboration, Ade P. A. R., Aghanim N. et al. 2016, Planck 2015 results. XIII. Cosmological Parameters, *A&A*, 594, A13
- Ricci, C., Trakhtenbrot, B., Koss, M. J., et al. 2017, BAT AGN Spectroscopic Survey. V. X-ray Properties of the Swift/BAT 70-month AGN Catalog, *ApJS*, 233, 17
- Schlafly, E. F., & Finkbeiner, D. P. 2011, Measuring Reddening with Sloan Digital Sky Survey Stellar Spectra and Recalibrating SFD, *ApJ*, 737, 103
- Schmidt, M., & Green, R. F. 1983, Quasar Evolution Derived from the Palomar Bright Quasar Survey and other Complete Quasar Surveys, *ApJ*, 269, 352
- Tremaine, S., Gebhardt, K., Bender, R., et al. 2002, The Slope of the Black Hole Mass versus Velocity Dispersion Correlation, *ApJ*, 574, 740
- Vanden Berk, D. E., Richards, G. T., Bauer, A., et al. 2001, Composite Quasar Spectra from the Sloan Digital Sky Survey, *AJ*, 122, 549
- van Dokkum, P. G. 2001, Cosmic-Ray Rejection by Laplacian Edge Detection, *PASP*, 113, 1420
- Vestergaard, M., & Peterson, B. M. 2006, Determining Central Black Hole Masses in Distant Active Galaxies and Quasars. II. Improved Optical and UV Scaling Relationships, *ApJ*, 641, 689
- Volonteri, M., & Rees, M. J. 2005, Rapid Growth of High-Redshift Black Holes, *ApJ*, 633, 624
- Woo, J.-H., Treu, T., Malkan, M. A., & Blandford, R. D. 2008, Cosmic Evolution of Black Holes and Spheroids. III. The $M_{\text{BH}}-\sigma_*$ Relation in the Last Six Billion Years, *ApJ*, 681, 925
- Xie, Y., Ho, L. C., Zhuang, M.-Y., et al. 2021, The Infrared Emission and Vigorous Star Formation of Low-redshift Quasars, *ApJ*, 910, 124
- Yu, Q., & Tremaine, S. 2002, Observational Constraints on Growth of Massive Black Holes, *MNRAS*, 335, 965
- Zhao, Y., Ho, L. C., Shangguan, J., et al. 2021, The Diverse Morphology, Stellar Population, and Black Hole Scaling Relations of the Host Galaxies of Nearby Quasars, *ApJ*, 911, 94
- Zhao, D., Ho, L. C., Zhao, Y., et al. 2019, The Role of Major Mergers and Nuclear Star Formation in Nearby Obscured Quasars, *ApJ*, 877, 52
- Zhuang, M.-Y., & Ho, L. C. 2020, The Interplay between Star Formation and Black Hole Accretion in Nearby Active Galaxies, *ApJ*, 896, 108
- Zhuang, M.-Y., Ho, L. C., & Shangguan, J. 2021, Black Hole Accretion Correlates with Star Formation Rate and Star Formation Efficiency in Nearby Luminous Type 1 Active Galaxies, *ApJ*, 906, 38

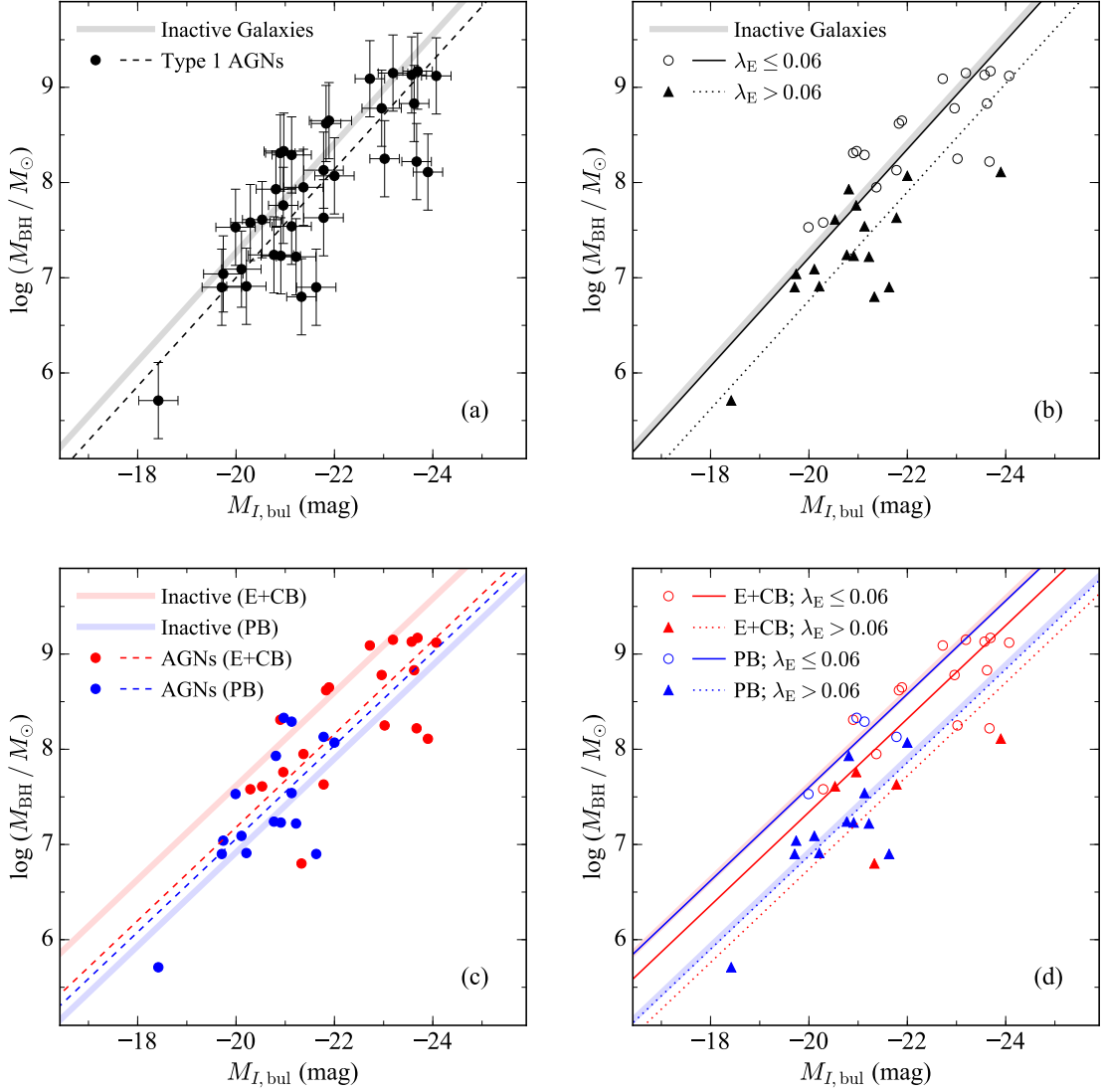


Figure 3. Relations between BH mass (M_{BH}) and absolute I -band bulge magnitude ($M_{I, \text{bul}}$) for type 1 AGNs. In all panels, shaded line denotes the relation of inactive galaxies from Kormendy & Ho (2013). (a) Filled circles and the dashed line denote type 1 AGNs and their relation. (b) Open circles (filled triangles) and solid line (dashed line) represent AGNs with low (high) Eddington ratio and their relation, respectively. (c) The sample is divided into two subgroups according to bulge types. Blue shaded (red shaded) line denotes the relation of pseudo-bulges (ellipticals and classical bulges) in inactive galaxies. Red (blue) circles and dashed line denotes AGNs with ellipticals and classical bulges (pseudo-bulges) and their relation, respectively. (d) Red (blue) circles and solid line denote ellipticals and classical bulges (pseudo-bulges) with low Eddington ratio in our sample and their relation, respectively. Red (blue) triangles and dotted line denote ellipticals and classical bulges (pseudo-bulges) with high Eddington ratio in our sample and their relation, respectively.

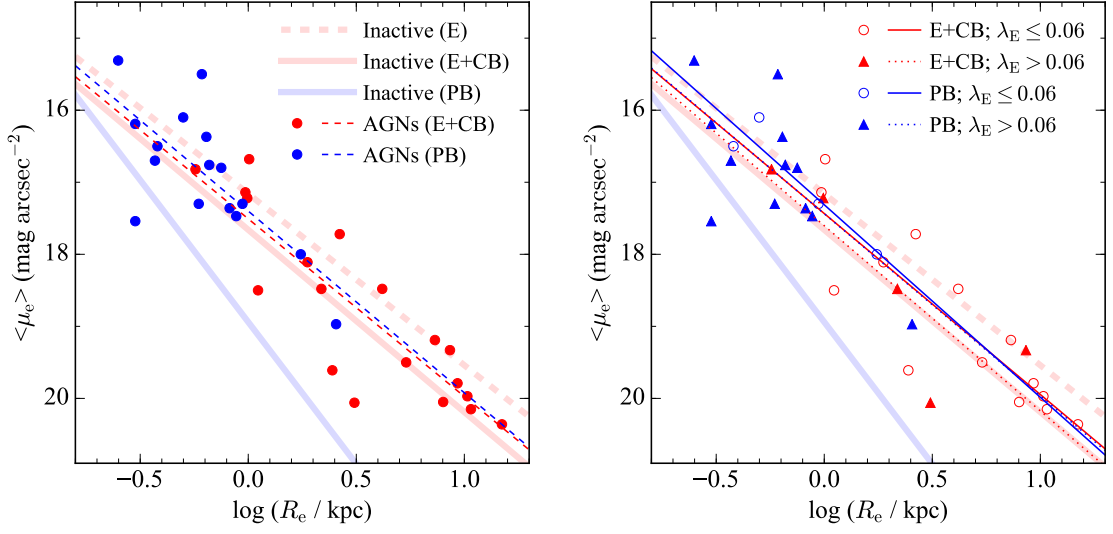


Figure 4. Relation between effective radius (R_e) and mean surface brightness ($\langle \mu_e \rangle$) within R_e for type 1 AGNs. The sample is divided into two subsamples according to bulge types (left) and four subgroups according to bulge types and Eddington ratio (right). For both panels, red (blue) symbols and lines denote ellipticals and classical bulges (pseudo-bulges). Kormendy relations for inactive galaxies adapted from Kim & Ho (2019) are shown by thick shaded lines. Kormendy relation for elliptical galaxies from Gao et al. (2020) is denoted by thick red dashed line. In the left panel, red and blue dashed lines represent the Kormendy relations for AGNs with ellipticals and classical bulges and those with pseudo-bulges, respectively. In the right panel, AGNs with low (high) Eddington ratio and their Kormendy relation are denoted by open circles (filled triangles) and solid (dotted) lines, respectively.

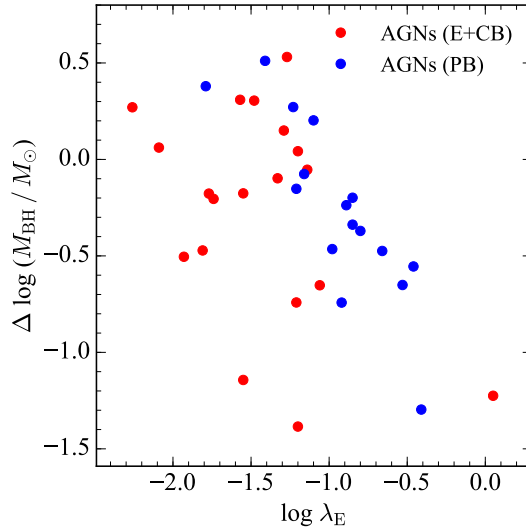


Figure 5. Comparison of Eddington ratio (λ_E) with BH mass offset ($\Delta \log M_{\text{BH}}$) from the $M_{\text{BH}}-M_{I,\text{bul}}$ relation of inactive galaxies. BH mass offset of type 1 AGNs is calculated by subtracting the virial BH mass estimates from that inferred from the $M_{\text{BH}}-M_{I,\text{bul}}$ relation of inactive galaxies at a given bulge luminosity. Type 1 AGNs hosted by ellipticals and classical bulges are plotted as filled red circles, while those hosted by pseudo-bulges are plotted as filled blue circles.